

Multi-epoch analysis of the X-ray spectrum of the active galactic nucleus in NGC 5506

Shangyu Sun¹, Matteo Guainazzi², Qingling Ni¹, Jingchun Wang¹, Chenyang Qian¹,
Fangzheng Shi¹, Yu Wang¹, Cosimo Bambi^{1,3*}

¹ Center for Field Theory and Particle Physics and Department of Physics, Fudan University, 220 Handan Road, Shanghai 200433, China

² ESTEC/ESA, Keplerlaan 1, 2201AZ Noordwijk, The Netherlands

³ Theoretical Astrophysics, Eberhard-Karls Universität Tübingen, Auf der Morgenstelle 10, 72076 Tübingen, Germany

13 April 2017

ABSTRACT

We present a multi-epoch X-ray spectroscopy analysis of the nearby narrow-line Seyfert I galaxy NGC 5506. For the first time, spectra taken by *Chandra*, *XMM-Newton*, *Suzaku*, and *NuSTAR* - covering the 2000–2014 time span - are analyzed simultaneously, using state-of-the-art models to describe reprocessing of the primary continuum by optical thick matter in the AGN environment. The main goal of our study is determining the spin of the supermassive black hole (SMBH). The nuclear X-ray spectrum is photoelectrically absorbed by matter with column density $\simeq 3 \times 10^{22} \text{ cm}^{-2}$. A soft excess is present at energies lower than the photoelectric cut-off. Both photo-ionized and collisionally ionized components are required to fit it. This component is constant over the time-scales probed by our data. The spectrum at energies higher than 2 keV is variable. We propose that its evolution could be driven by flux-dependent changes in the geometry of the innermost regions of the accretion disk. If we take this hypothesis into account, the black hole spin in NGC 5506 is constrained to be comprised between $0.91 < a < 0.98$ at 90% confidence level for one interesting parameter.

Key words: Galaxies: active - Galaxies: Individual: NGC 5506 - Accretion, accretion discs

1 INTRODUCTION

NGC 5506 is a nearby ($z=0.0062$; ~ 24 Mpc) edge-on Sa galaxy within the local Virgo supercluster, hosting an active galactic nucleus (AGN) classified as radio-quiet narrow-line Seyfert I (NLSy1; Nagar et al. 2002). The NLSy1 galaxies generally have lower SMBH masses and higher accretion rates (Komossa & Xu 2007). NGC 5506 is an obscured AGN but still Compton-thin ($N_H \approx 3 \times 10^{22} \text{ cm}^{-2}$; Wang et al. 1999). Its brightness in X-ray makes it a proper source for studying in detail the high-energy activities near an active SMBH of this kind.

The hard X-ray ($E > 2$ keV) emission from an radio-quiet AGN (without any prominent jet) originates primarily from the vicinity of the central engine, the SMBH, as close as a few tens of gravitational radii, r_g away from the event horizon ($r_g = GM/c^2$; gravitational radius) as suggested by the short variability timescales in hard X-ray band (e.g., Grandi et al. 1992; McHardy et al. 2006; Uttley 2007; Zoghbi et al. 2013). In this innermost region of AGN, the accretion disc (AD), whose blackbody radiation spec-

trum peaks around ultra-violet (UV) wavelengths, is illuminated by a hard X-ray source. The spectrum of this hard X-ray source is typically described by a power-law function with a high-energy cutoff. The hard X-ray source can be a magnetically dominated corona residing above the surface of the disc (e.g., Galeev et al. 1979; Haardt & Maraschi 1991; Haardt et al. 1994; Di Matteo 1998; Merloni & Fabian 2001). Compton scattering, fluorescence and photoelectric absorption occur in the AD, creating the so called "reflection spectrum" (George & Fabian 1991). The AD thermal photons are also inverse-Compton up-scattered by relativistic electrons. Iron fluorescence in a dense and relatively cold medium (e.g., Barr et al. 1985; Nandra et al. 1989; Pounds et al. 1990; George & Fabian 1991; Nandra & Pounds 1994) can bring an emission line at about 6.4 keV. The shape of the Fe K α line includes the information of the Doppler shifts caused by the reflection if produced in a relativistically rotating AD, the photon propagation in a curved space-time and gravitational redshift caused by the (possibly fast spinning) SMBH (Fabian et al. 1989; Laor 1991). These relativistically broadened Fe K α lines in AGN spectra have been resolved by *Chandra*, *XMM-Newton*, *Suzaku*, and *NuSTAR* (e.g., Ballantyne et al. 2003; Reynolds & Nowak 2003;

* Corresponding author: bambi@fudan.edu.cn

Miller 2007; Nandra et al. 2007; Fabian et al. 2009; Nardini et al. 2012; Walton et al. 2012, 2013; Risaliti et al. 2013; Parker et al. 2014; Madsen et al. 2015). The spectral analysis of relativistically broadened lines can provide a measurement of the black hole spin (e.g., Brenneman & Reynolds 2006; Reynolds & Fabian 2008; Parker et al. 2014) and potentially even test Einstein’s gravity (Bambi 2015; Jiang et al. 2015).

In the soft X-ray band, an excess over the extrapolation of the absorbed nuclear emission has been observed in many obscured AGN spectra. The origin of this *soft excess* is complex. The AGN nuclear emission can heat up its circumnuclear gas, and can result in narrow radiative recombination continua (RRC) as well as recombination lines of highly-ionised atomic species. This kind of photoionized spectra have been found in several sources, e.g., the Circinus Galaxy (Sambruna et al. 2001), Mrk 3 (Sako et al. 2000; Bianchi et al. 2005; Pounds & Page 2005), NGC 1068 (Kinkhabwala et al. 2002; Young et al. 2001), NGC 4151 (Schurch et al. 2004). In a *XMM-Newton* survey of obscured AGNs (Guainazzi & Bianchi 2007), photoionization signature was found in 36% of the sample. The line widths of RRC show plasma temperatures of $\sim eV$ (Kinkhabwala et al. 2002). In the spectra of some obscured AGNs, higher order transitions are enhanced with respect to pure photoionization. In these cases, resonant scattering is important in the balance between photoionization and photoexcitation. Alternatively, shocks produced by AGN outflows (King 2005) or starburst (Storchi-Bergmann et al. 1998; González Delgado et al. 2001) can also heat up ambient gas to $\sim 10^6$ K. A spectrum of collisionally ionized plasma is characteristic for these scenarios (Viegas-Aldrovandi & Contini 1989), but it contributes to observed soft X-ray emission only in galaxies with strong nuclear star formation (Guainazzi et al. 2009).

Bianchi et al. (2003) analyzed NGC 5506 X-ray spectra taken from 1997 to 2002, reporting only a narrow Fe K α line. However, deeper *XMM-Newton* observations unveiled a moderately broadened component of the Fe K α line (Guainazzi et al. 2010a). Furthermore, the spectrum observed by *NuSTAR*, which has a high sensitivity above 10 keV, constrained the high-energy cutoff of the continuum (Matt et al. 2015). In this paper, we analyze for the first time all the good quality X-ray archival data of NGC 5506. The main goal of this paper is achieving the most accurate determination so far of the relativistic accretion disk and black hole parameters, taking advantage of the unprecedented combination of signal-to-noise ratio and energy broadband coverage (0.2–79 keV).

In Sect. 2, we report the observations and data products from each instrument. In Sect. 3, we show the procedures and results on the spectral analysis. Then we discuss and conclude in Sect. 4.

2 OBSERVATIONS AND DATA PRODUCTS

For the sake of this work, 11 deep observations (exposure time > 20 ks) in X-rays were selected from NASA’s High Energy Astrophysics Science Archive Research Center (HEASAC). The observation time, id, exposure time, start time, and its corresponding epoch name used in this work (E1–E11) are listed in Table 1.

2.1 *XMM-Newton*

The data from European Photon Imaging Camera (EPIC)-Metal Oxide Semi-conductor (MOS; Turner et al. 2001) and pn (Strüder et al. 2001) were reduced using the software SAS provided by ESA (Gabriel et al. 2004). Flaring particle background

was filtered using light curves extracted at high energies (Principal Investigator (PI) > 10 keV for MOS and PI between 10 keV and 12 keV for PN) and with single events only. We removed the high particle background intervals above the appropriate count rate thresholds (see Table 2) individually set for each observation and each instrument (Guainazzi et al. 2010a). We selected single, double, triple and quadruple events for MOS; single and double events for PN. Source spectra were extracted from circular regions around the source centroid. For MOS data, background spectra were extracted from annulus region with no extra sources around the same centroid as the corresponding source spectra. For PN, background spectra were extracted from the circular regions at the same height in detector coordinates to ensure the same charge transfer inefficiency correction as the source spectra. The redistribution matrix and the effective area were computed through the SAS tasks, ARFGEN and RMFGEN. The spectral energy range used in this work is 1–10 keV.

Data from reflection grating spectrometer (RGS) were processed with SAS v.14.0.0, by using the standard task pipeline RGSPROC. The spectral energy range used in this work is 0.2–2 keV.

2.2 *Suzaku*

The *Suzaku* data were reduced by software package HEASOFT v6.16, using the AEPipeline script following the *Suzaku ABC Guide*¹ to perform reprocessing (update energy calibration) and re-screening.

As for the X-ray imaging spectrometer (XIS) data, we extract spectra using a 260'' region around the source through XSELECT. The ancillary response matrices (ARFs) and the detector response matrices (RMFs) were generated by XISRmfGEN and XISARFGEN task pipelines, respectively. The task pipeline ADDASCASPEC was used to combine front-side illuminated spectra and responses. The spectra from XIS0, XIS2, and XIS3 are combined for each observation and referred to in the following as ‘front-side illuminated spectra’. The spectrum from XIS1 is referred to in the following as ‘back-side illuminated spectrum’. The spectral energy range used in this work is 0.5–10 keV.

The data from the hard X-ray detector (HXD) include those from gadolinium silicate crystal counters (Gd₂SiO₅(Ce); GSO; >50 keV) and from the silicon PIN diodes (< 50 keV). In this work, only PIN data are used, while NGC 5506 was not detected by the GSO. The PIN data was reduced by standard task pipeline HXDPINXBPI. The spectral energy range used in this work is 10–50 keV.

2.3 *NuSTAR*

The data from focal-plane modules (FPM) 1 and 2 were reduced with HEASOFT v6.16, calibration files of INDX20150316. The NUPIPELINE and NUPRODUCTS tasks were run. Source spectra were extracted from a circular region with radius 2'. An off-source background region of the same size was used. The two regions were separated by 1'. The spectral energy range used in this work is 5–79 keV.

¹ It can be found at <https://heasarc.gsfc.nasa.gov/docs/suzaku/analysis/abc/>.

Table 1. Log of the observations discussed in this paper.

Observatory	obsid	exposure time [s]	start time [yyyy-mm-dd hh:mm:ss]	epoch index
<i>Chandra</i>	1598	90040	2000-12-31 06:21:12	E01
<i>XMM-Newton</i>	0013140101	20007	2001-02-02 22:01:45	E02
<i>XMM-Newton</i>	0201830201	21617	2004-07-11 09:47:01	E03
<i>XMM-Newton</i>	0201830301	20409	2004-07-14 22:11:39	E04
<i>XMM-Newton</i>	0201830401	21956	2004-07-22 13:07:37	E05
<i>XMM-Newton</i>	0201830501	20411	2004-08-07 20:17:40	E06
<i>Suzaku</i>	701030010	47753	2006-08-08 16:30:05	E07
<i>Suzaku</i>	701030020	53296	2006-08-11 02:26:18	E08
<i>Suzaku</i>	701030030	57406	2007-01-31 02:12:12	E09
<i>XMM-Newton</i>	0554170101	88919	2009-01-02 19:32:26	E10
<i>NuSTAR</i>	60061323002	56585	2014-04-01 23:41:07	E11

Table 2. Parameters for EPIC data reduction.

ObsID	C_{th}^a [s ⁻¹]	R_s^b [arcsec]
0013140101	0.2 / 0.5	100 / 40
0201830201	0.5 / 0.5	42 / 45
0201830301	0.5 / 0.35	40 / 42
0201830401	0.35 / 0.35	40 / 42
0201830501	0.35 / 0.35	40 / 42
0554170101	0.35 / 0.35	50 / 50

^a Threshold count rate on the high-energy, single-event light curve to identify intervals of high particle background in MOS/PN, respectively.

^b R_s Radius for the source spectrum extraction region.

2.4 *Chandra*

The *Chandra* high energy grating (HEG) and medium energy grating (MEG) spectra in this work were extracted from the *Chandra Grating-Data Archive and Catalog* (TGCat). Details on the data reduction can be found in [Huenemoerder et al. \(2011\)](#). The spectral energy ranges used in this work are 0.4–5 keV for the two medium energy grating (MEG) spectra, and 0.8–10 keV for the two high energy grating (HEG) spectra.

2.5 Re-binning spectra

Spectra were re-binned to ensure that each background-subtracted energy channel had at least one count, and to sample the instrumental energy resolution according to the prescription in [Kaastra & Bleeker \(2016\)](#).

2.6 Evolution across 11 epochs

Fig. 1 illustrates the X-ray spectral variability in NGC 5506 from epoch 1 to 11. Variability is observed only above 1.3 keV. At about 2.5 keV, the spectrum change by a factor of 2.5 between the highest and lowest state. These multi-epoch spectra can be classified into three states according to the flux level: high states (A) including E06–E10, intermediate states (B): E01–E05, low state (C): E11. NGC 5506 evolved from intermediate states (E01–E05), to high states (E06–E10), and reached finally a low state (E11).

3 SPECTRAL RESULTS

The spectral fits are performed using XSPEC v.12.8.2 ([Arnaud 1996](#)). The statistical uncertainties reported in this paper corresponds to 90% confidence level for one interesting parameter.

3.1 The soft X-ray spectrum

In order to achieve a broad-band modeling of the NGC5506 X-ray spectra, we considered initially the soft X-ray band ($E < 1.3$ keV) only. Our working hypothesis is that soft X-rays are dominated by emission due to diffuse gas associated to extended Narrow Line Regions, while emission at higher energy is dominated by the nuclear emission. Different models of the soft X-ray spectrum are compared in Tab. 3. Comparing models of increasing level of complexity via the F-test, we define the best-fit baseline model of the soft X-ray spectrum as: POWERLAW[1] + XSTAR2XSPEC + APEC[1] + APEC[2] to model the soft X-ray component. Each component is described in the following.

- XSTAR2XSPEC (NGC5506) is an additive table model generated by XSTAR. XSTAR ([Kallman & Bautista 2001](#)) calculates the physical conditions and emission spectra of photoionized gases. It is parameterized by a column density $N_H^{phot.}$ and ionisation $\xi_{phot.}$. PEGPWRLW is a power-law component (with photon index $\alpha_{phot.}$) approximating free electron scattering in the photoionized gas. APEC ([Smith et al. 2001](#)) components are emission spectra from collisionally-ionized diffuse gases of temperatures $kT_1^{coll.}$ and $kT_2^{coll.}$ calculated using the ATOMDB code v2.0.2.² All parameters mentioned in this paragraph are left epoch-invariant. The best-fit parameters are shown in Tab. 5.

To test if the soft X-ray emission is constant during our observations (as expected on astrophysical grounds; see Sect. 1), RGS spectra of each epoch were fit using the aforementioned model. Constant-functions were fit to soft X-ray parameters as a function of time, and then the probability of the validity of this assumption was calculated. The results of this test are reported in Tab. 4. The high p -values of fits suggest that invariant model parameters describe the soft RGS spectra properly. To reduce the statistical uncertainties in RGS measurements, spectra from different epochs were merged. Hereafter, the parameters of the model describing the soft X-ray band are assumed to be epoch-independent.

² <http://atomdb.org/>

NGC5506

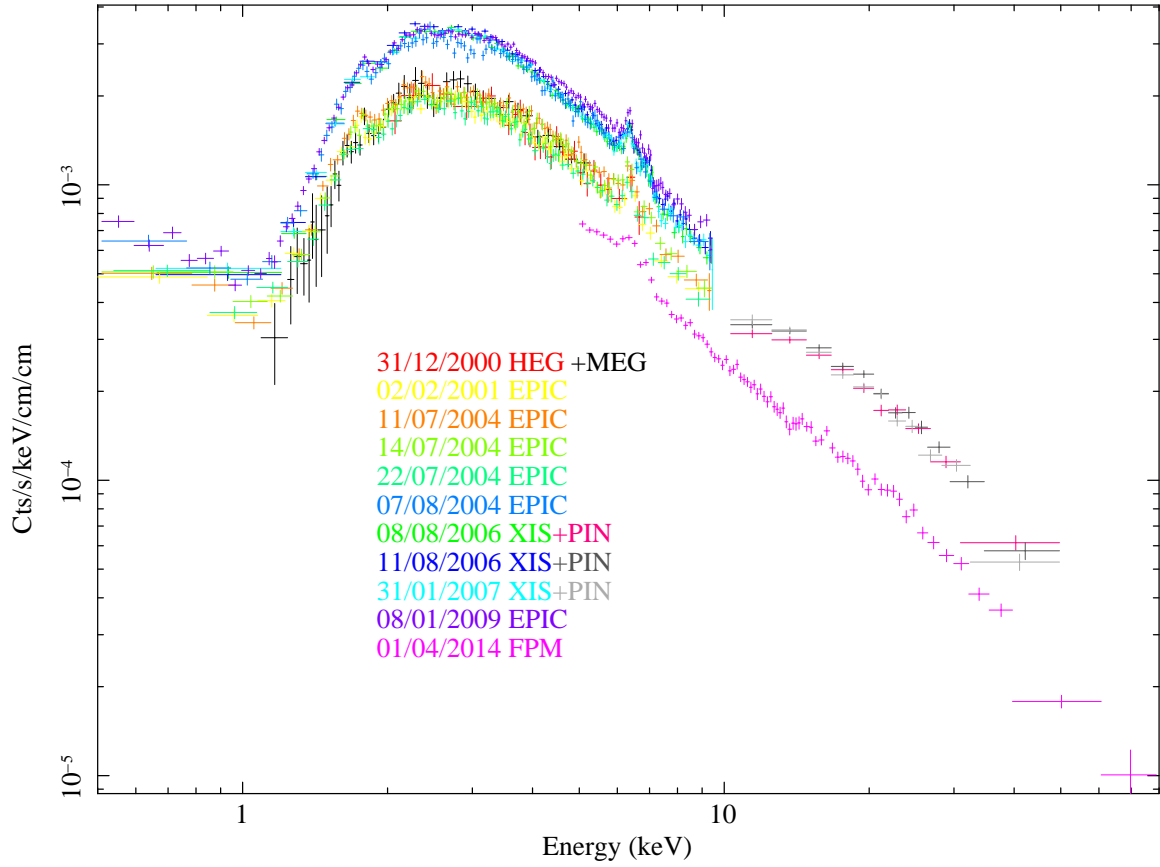


Figure 1. NGC 5506 count spectra from *Chandra*, *XMM-Newton*, *Suzaku*, and *NuSTAR* (corrected by effective areas). The observation dates, instruments, and corresponding colors are labeled in the figure. The intrinsic variability of the source at energies > 2 keV can be directly seen. For example, at 3 keV EPIC spectra from 08/01/2009 and 14/07/2004 are different by a factor of ~ 2 .

Table 3. Models for high-resolution spectra below 1.3 keV.

model	C-Statistic	$\chi^2 n.d.f.$	F-test prob. [♣]
A(nucl.)	18593	16847/5496=3.065	–
B(nucl. + coll.)	6771	6412/5493=1.167	4.0×10^{-17} [A]
C(nucl. + phot.)	6356	6185/5491=1.126	9.5×10^{-11} [A]
D(nucl. + phot. + coll.)	6186	6071/5488=1.106	3.6×10^{-8} [C]
E(nucl. + phot. + 2 coll.)	6160	6030/5485=1.099	2.2×10^{-7} [D]

A: TBABS[1] * (TBABS[2]*POWERLAW[2])

B: TBABS[1] * (APEC + TBABS[2]*POWERLAW[2])

C: TBABS[1] * (POWERLAW[1] + XSTAR2XSPEC + TBABS[2]*POWERLAW[2])

D: TBABS[1] * (POWERLAW[1] + XSTAR2XSPEC + APEC + TBABS[2]*POWERLAW[2])

E: TBABS[1] * (POWERLAW[1] + XSTAR2XSPEC + APEC[1] + APEC[2] + TBABS[2]*POWERLAW[2])

See description for each model in Subsect. 3.1.

number of PHA bins: 5500

♣ the probability that the hypothesized model is worse; comparing with the null model in []

3.2 Broadband X-ray modeling

We then fit the X-ray broadband spectra of the 11 epochs with the following model:

CONST*TBABS1*PEGPWRLW + APEC1 + APEC2 + XSTAR2XSPEC
+TBABS2*RELXILL + MT_{sca} + MT_{lin}

Table 4. Constant-function fitting to RGS epoch-dependent parameters

parameter	$\chi^2 n.d.f.$	p-value
α_{phot}	4.07/5	0.539
kT_1^{coll}	3.64/5	0.603
Z	0.65/5	0.986
kT_2^{coll}	0.50/5	0.992
$\log \xi_{\text{phot}}$	4.97/5	0.420

number of entries: 6 (epochs)

number of parameter: 1 (constant-function)

See description for each parameter in Subsect. 3.2.

XSTAR2XSPEC, PEGPWRLW, and APEC, are explained in Sect. 3. The other components are described in the following.

• MYTORUS³ (Murphy & Yaqoob 2009) was used to calculate the reflection and scattering from optically thick matter in a toroidal geometry surrounding the AGN. In this work, this torus model set includes MT_{sca} and MT_{lin}. MT_{sca} calculates the scattered continuum. It is the collection of all escaping photons that have been scattered in the medium at least once. It is also referred to as the

³ <http://mytorus.com/>

reflection spectrum. MT_{in} calculates the fluorescent emission-line spectrum, which is produced by the zeroth-order (or unscattered) component resulting from the absorption of a continuum photon above the K-edge threshold as well as by the emission-line photons that are scattered before they escape the medium. It includes the Compton shoulder of the observed emission line. The column density of the reprocessing matter $N_{\text{H}}^{\text{torus}}$, the inclination angle θ_{torus} , and the photon index of the reprocessed primary continuum α_{torus} , are assumed epoch-invariant, following Guainazzi et al. (2010a).

- RELXILL (Dauser et al. 2014; García et al. 2014) describes an X-ray source of a power-law photon index $\alpha_{\text{coro.}}$ and a cutoff at high energies $E_{\text{cut}}^{\text{coro.}}$ plus the X-ray reflection from a relativistically rotating disk in a strong gravitational field generated by a (possibly spinning) black hole. We assumed that the emission occurs in an annulus over the accretion disk, whose outer radius was fixed to $400 r_g$, and whose inner radius coincides with the innermost stable circular orbit (ISCO), which is a function of the BH spin a (Bardeen et al. 1972). We assumed that the radial profile of the emissivity function can be described by a single power-law of index β_{AD} . The inclination angle of the AD is θ_{AD} . The definition of parameter *reflection fraction* $F_{\text{refl.}}$ can be found in (Dauser et al. 2014). The following astrophysical parameters: $\alpha_{\text{coro.}}$, β_{AD} , ionisation parameter of AD ξ_{AD} , and normalisation of RELXILL $N_0^{\text{RELX.}}$ are assumed independently variable in each epoch, while the other parameters are left epoch-invariant.

- CONST represents the cross-instrument calibration factors. TBABS[2] describes the obscuration of the nuclear emission by a hydrogen column density $N_{\text{H}}^{\text{nucl.}}$. TBABS[1] describes obscuration due to intervening gas in our Galaxy by a hydrogen column density $N_{\text{H}}^{\text{gala.}}$. All parameters mentioned in this paragraph are left epoch-invariant except $N_{\text{H}}^{\text{nucl.}}$.

- We assumed a variable and epoch-invariant elemental abundance Z . Its value is assumed to be consistent across models (APEC[1], APEC[2], and RELXILL).

3.2.1 fit results

Spectra are shown epoch by epoch in the upper panels of Figs. 2 to 3, and their data/model ratios in the lower panels.

The the best-fit results of stable (epoch-invariant) astrophysical properties are listed in Tab. 5. The parameters that vary with epochs and drive the evolution of the spectrum are in Tab. 6.

3.2.2 nuclear emission

In this paper, we employed the state-of-the-art RELXILL model to model the reflection spectrum due to the X-ray illuminated relativistic accretion disk. This allows us to obtain statistical constraints on: a BH of spin $0.97 \pm_{0.010}^{0.0082}$ with an AD inclination angle $41 \pm_{-0.18}^{+0.12}$, emissivity indices varying from 1.2 to 8.5, ionisation parameter $\log(\xi_{\text{AD}})$ varying in the range 1.6 to above 4.7, a corona of photo-index varying between 1.7–2.1, and a high-energy cutoff ~ 500 keV. The reflection fraction is ~ 1.3 (implying the corona residing $\sim 20 r_g$ above the black hole⁴).

We compare our results with those in other studies: in the paper of Matt et al. (2015) (NGC 5506 by *NuSTAR*), the AD inclination angle was reported as $< 44^\circ$, consistent to what derived in this work; ionisation $\xi = 22 \pm_{-7}^{+15}$, which is smaller than that for

⁴ converted through the plot of “reflection fraction v.s. height of corona” in Dauser et al. (2016).

Table 5. Fit results of epoch-independent parameters.

Par. name	Par. unit	best-fit value
$N_{\text{H}}^{\text{gala.}}$	cm^{-2}	$3.6 \pm_{0.072}^{0.10} \times 10^{-21}$
$\alpha_{\text{phot.}}$		$2.8 \pm_{0.16}^{0.13}$
$kT_1^{\text{coll.}}$	keV	$6 \pm_{0.7}^{0.2} \times 10^{-2}$
Z	solar abundance	$5.4 \pm_{0.10}^{0.15} \times 10^{-1}$
$kT_2^{\text{coll.}}$	keV	$3.0 \pm_{0.14}^{0.13} \times 10^{-1}$
$\log \xi_{\text{phot.}}$		$1.8 \pm_{0.16}^{0.10}$
a		$9.7 \pm_{0.10}^{0.082} \times 10^{-1}$
θ_{AD}	deg	$4.1 \pm_{0.018}^{0.012} \times 10^1$
$E_{\text{cut}}^{\text{coro.}}$	keV	$5.0 \pm_{0.13}^{0.10} \times 10^2$
$F_{\text{refl.}}$		$1.3 \pm_{0.024}^{0.010}$
$N_{\text{H}}^{\text{torus}}$	cm^{-2}	$5 \pm_{0.3}^{0.1} \times 10^{24}$
θ_{torus}	deg	$4.7 \pm_{0.19}^{0.10} \times 10^1$
α_{torus}		$2.0 \pm_{0.015}^{0.010}$
E_1^{line}	keV	$1.7 \pm_{0.072}^{0.023}$
σ_1^{line}	keV	$1 \pm_{0.2}^{0.1} \times 10^{-1}$
E_2^{line}	keV	$6.7 \pm_{0.10}^{0.18}$
σ_2^{line}	keV	$2.2 \pm_{0.042}^{0.050} \times 10^{-1}$

★ See description for each parameter in Subsect. 3.2.

E11 in this work ($\log \xi \sim 4.5$); corona photo-index 1.9, which is harder than that for E11 in this work; a very high-energy cutoff at $720 \pm_{-190}^{+130}$ keV, which is higher than in this work, but still consistent with our results.

The radial index of the emissivity profile exhibits large errors. A test of making this parameter epoch-independent was performed. There was no great change in data-model residuals of each spectrum. The value of C-Statistic increased by 199, while the number of parameters decreased by 11. C-Statistic/d.o.f: 12443/10154 = 1.225 (original); 12642/10165 = 1.244 (this test). A F-test was made to compare these two hypotheses. The restricted hypothesis (the index epoch-invariant) has a Chi-Squared of 11662 and a number of free parameters 99 (d.o.f 10165) while the unrestricted hypothesis (epoch-variant) has a Chi-Squared of 11498 and a number of free parameters 110 (d.o.f 10154). We found that the hypothesis of epoch-dependent β_{AD} is better with a confidence level of more than 99%.

Suzaku/XIS spectra show positive residuals at ~ 7 keV (see an example of this feature in Fig. 4). This might be the signature of emission from resonant H-like iron lines. Therefore, we added a further, unresolved Gaussian profile to the model, constraining its rest-frame centroid energy to be comprised between 6.6 and 7 keV. The value of goodness-of-fit (C-Statistic) decreased by 190, while the number of free parameters increased by 3. C-Statistic/d.o.f:

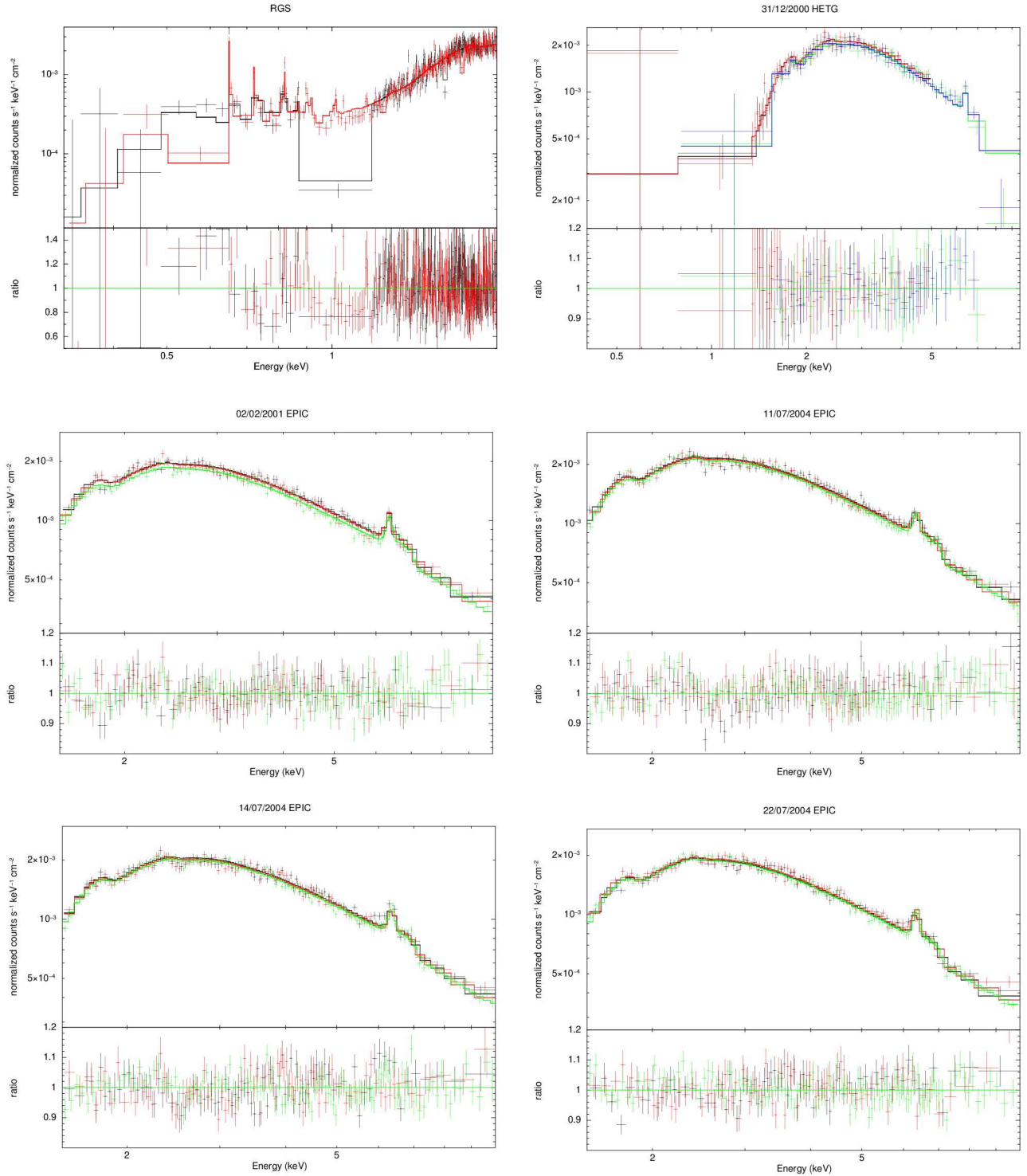


Figure 2. *Upper panels:* NGC 5506 X-ray spectra from RGS and Epochs 1–5, and their best-fit models. The instrument name and observation date for each epoch are on the top the panel. *Crosses:* data; *histogram lines:* models. *Lower panels:* the data/model ratios.

$12443/10154 = 1.225$ (original); $12253/10151 = 1.207$ (this test, adding a Gaussian profile). A F-test was made to compare these two hypotheses. The restricted hypothesis (without a Gaussian profile) has a Chi-Squared of 11498 and a number of free parameters 110 (d.o.f 10154) while the unrestricted hypothesis (with a Gaussian profile) has a Chi-Squared of 11336 and a number of free param-

eters 113 (d.o.f 10151). We found that the model with this Gaussian profile is better at a confidence level of larger than 99%.

In Figs. 5 and 6, we show the *NuSTAR* residuals once the normalisation of the RELXILL reflection component is set to zero, to show the effect that the relativistically smeared accretion disk reflection component has on the final best-fit model.

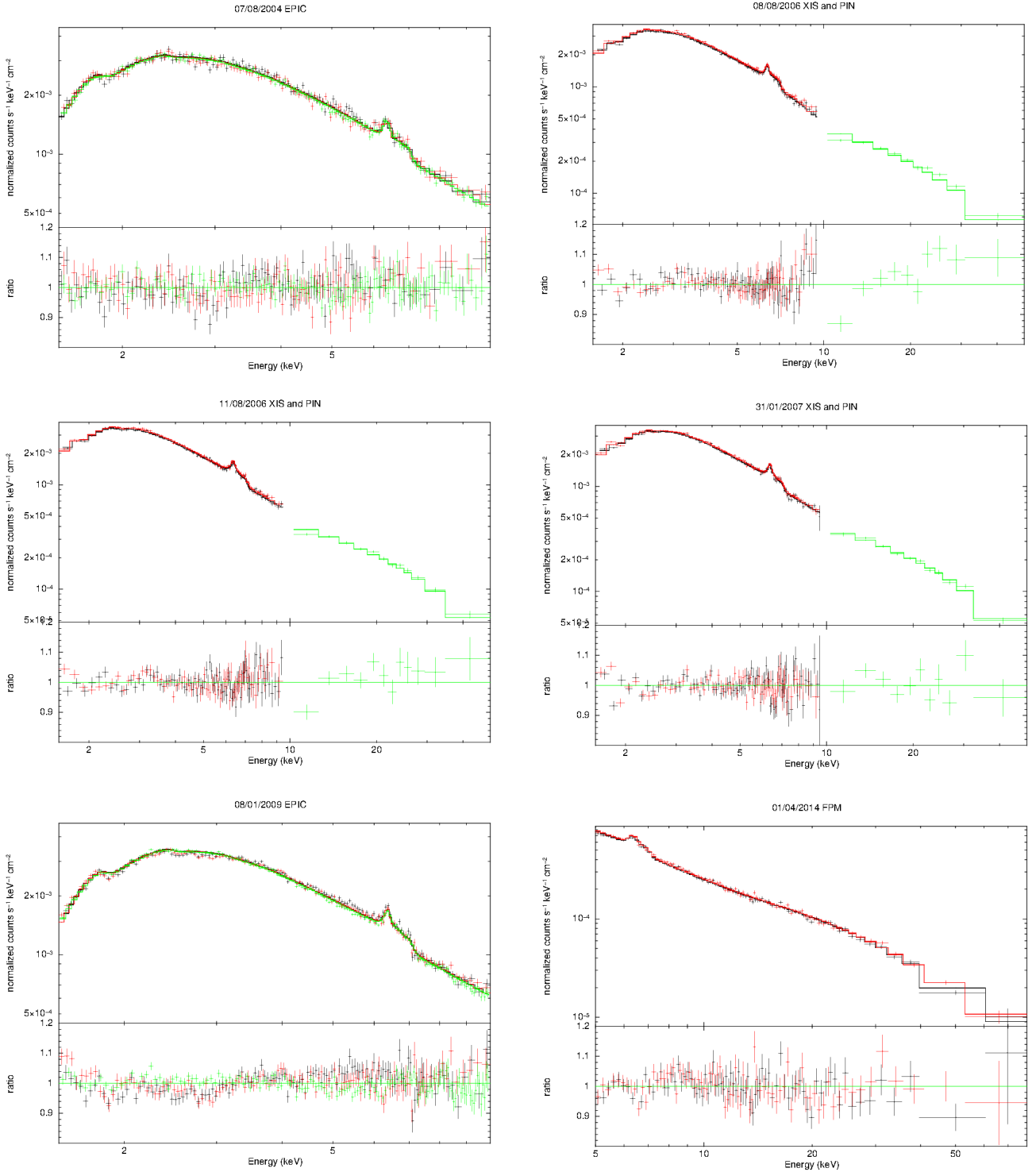


Figure 3. NGC 5506 X-ray spectra from Epochs 6–11, and their best-fit models. See description in the caption of Fig. 2.

A Gaussian profile at about 1.7 keV also is required by the fit. We do not have an explanation for this feature that we tentatively attribute to calibration uncertainties at the energies of the Si escape peak..

3.2.3 obscuration and torus

The column density of the nuclear absorber varies in the range $2.8\text{--}3.4 \times 10^{22} \text{ cm}^{-2}$. [Matt et al. \(2015\)](#) reported $3.1^{+0.21}_{-0.20} \times 10^{22} \text{ cm}^{-2}$, which agrees with the result in this work. *Ginga* also observed variation in the column density in a timescale of $\sim 1\text{--}10$ days in 1991 ([Bond et al. 1993](#)). This timescale is comparable with that presented in this paper, which corresponds to the coherent change

Table 6. Best-fit values of the time-dependent parameters.

epoch	start time [MJD]	energy flux (2–10 keV) [♣] [10^{-11} ergs $^{-1}$ cm $^{-2}$]	$N_{\text{H}}^{\text{nucl.}}$ [10^{22} cm $^{-2}$]	β_{AD}	$\alpha_{\text{coro.}}$	$\log \xi_{\text{AD}}$
E01	51909	$6.0 \pm_{0.041}^{0.042}$	$3.3 \pm_{0.017}^{0.017}$	$5.0 \pm_{0.81}^{0.89}$	$2.0 \pm_{0.051}^{0.010}$	$4.7 \pm_{0.13}^{0.15}$
E02	51942	$6.2 \pm_{0.030}^{0.030}$	$2.8 \pm_{0.031}^{0.023}$	$8.5 \pm_{0.32}^{0.11}$	$1.7 \pm_{0.042}^{0.010}$	$3.6 \pm_{0.14}^{0.48}$
E03	53197	$6.9 \pm_{0.030}^{0.030}$	$3.0 \pm_{0.056}^{0.013}$	$3.3 \pm_{0.45}^{0.53}$	$1.8 \pm_{0.057}^{0.010}$	$4.0 \pm_{0.13}^{0.67}$
E04	53200	$6.7 \pm_{0.030}^{0.031}$	$3.0 \pm_{0.011}^{0.024}$	$6.5 \pm_{0.81}^{0.89}$	$1.7 \pm_{0.010}^{0.019}$	$3.5 \pm_{0.11}^{0.10}$
E05	53208	$6.1 \pm_{0.029}^{0.029}$	$3.2 \pm_{0.024}^{0.021}$	$4.0 \pm_{0.56}^{0.95}$	$1.9 \pm_{0.010}^{0.041}$	$4.0 \pm_{0.15}^{0.10}$
E06	53234	$9.7 \pm_{0.036}^{0.036}$	$2.8 \pm_{0.058}^{0.010}$	$4.0 \pm_{0.33}^{0.36}$	$1.8 \pm_{0.028}^{0.0082}$	$3.5 \pm_{0.12}^{0.11}$
E07	53955	$9.8 \pm_{0.028}^{0.028}$	$3.1 \pm_{0.010}^{0.011}$	$2.0 \pm_{0.21}^{0.28}$	$2.0 \pm_{0.025}^{0.010}$	$1.6 \pm_{0.26}^{0.12}$
E08	53958	$10 \pm_{0.027}^{0.027}$	$3.1 \pm_{0.018}^{0.010}$	$1.2 \pm_{0.57}^{0.48}$	$1.7 \pm_{0.082}^{0.11}$	$3.0 \pm_{0.19}^{0.14}$
E09	54131	$9.9 \pm_{0.025}^{0.025}$	$3.2 \pm_{0.010}^{0.012}$	$1.6 \pm_{0.71}^{0.47}$	$2.1 \pm_{0.010}^{0.048}$	$3.8 \pm_{0.21}^{0.22}$
E10	54833	$11 \pm_{0.021}^{0.021}$	$3.1 \pm_{0.010}^{0.060}$	$2.6 \pm_{0.078}^{0.050}$	$1.9 \pm_{0.010}^{0.043}$	$3.2 \pm_{0.13}^{0.14}$
E11	56748	$5.8 \pm_{0.021}^{0.022}$	$3.4 \pm_{0.071}^{0.043}$	$3.5 \pm_{0.062}^{0.033}$	$2.1 \pm_{0.068}^{0.010}$	$4.5 \pm_{0.15}^{0.12}$

See description for each parameter in Subsect. 3.2.

♣ energy flux 2–10 keV calculated with spectrum by CFLUX in XSPEC

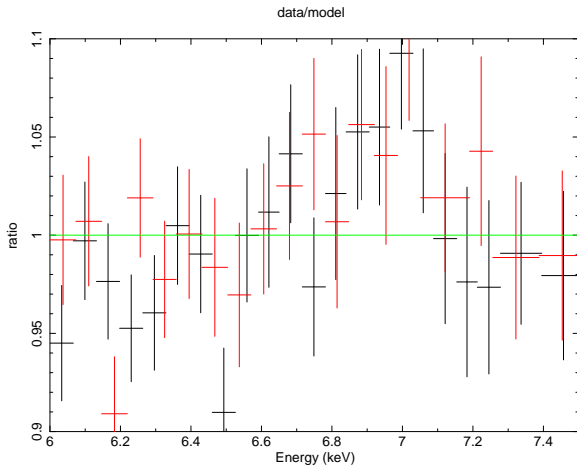


Figure 4. Data/model ratio when the baseline model is applied to the XIS spectra of Epoch E08 in the 6–7.5 keV energy range.

timescale of an astrophysical structure of $\sim 0.001\text{--}0.01$ pc. This size is similar to that of a broad-line region (BLR) of an AGN⁵.

The best-fit inclination angle of the torus is about 47° . The matter in the torus does not intercept the line of sight, and reflects the nuclear emission. The column density of the torus is $\sim 5 \times 10^{24}$ cm $^{-2}$. Note that this time-invariant column density is different from that on the LOS, $N_{\text{H}}^{\text{nucl.}}$.

Model TBABS[1] represents the medium with stable column density (3.6×10^{21} cm $^{-2}$) on the LOS from the outer soft-excess

⁵ A typical size of BLR of an AGN is $10^4 - 10^5 r_g$ (Netzer 2013); $r_g = GM/c^2$. In the case of NGC 5506, $\log(M_{\text{BH}}/M_\odot) = 7.95$ (Marinucci et al. 2012).

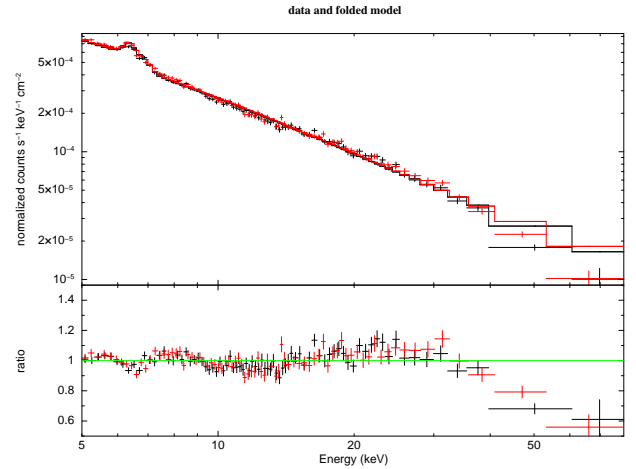


Figure 5. The FPM spectra and the best-fit model without the relativistic disk reflection component.

emitting region to the observer, including the medium causing the galactic extinction, inter-galactic medium, and galactic medium in NGC 5506.

3.3 Correlation results

Spearman's ranking correlation coefficients between several pairs of parameters were calculated and reported in Tab. 7. It is found that β_{AD} , $\log \xi_{\text{AD}}$, $\alpha_{\text{coro.}}$, $N_{\text{H}}^{\text{nucl.}}$ are all anti-correlated with the energy flux. The correlation between the column density and the photo-index is a degeneracy in the fit.

The fitting procedure employs C-Statistic (Cash 1979). The goodness-of-fit is 12260 for 10158 degrees of freedom.

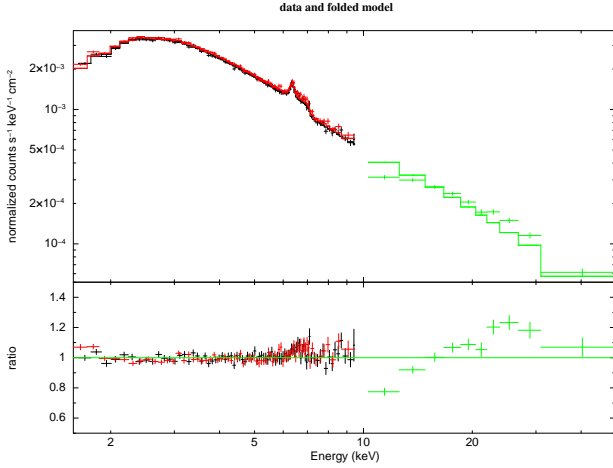


Figure 6. The XIS and PIN spectra from Epoch 7, and the best-fit model without the relativistic disk reflection component.

Table 7. Spearman’s ranking correlation coefficients between pairs of epoch-dependent parameters.

X	Y	ρ	two-tailed probability P-value
energy flux [♣]	$N_{\text{H}}^{\text{nucl.}}$	-0.314	0.347
energy flux [♣]	$\alpha_{\text{coro.}}$	-0.171	0.614
energy flux [♣]	β_{AD}	-0.702	0.016
energy flux [♣]	$\log \xi_{\text{AD}}$	-0.781	0.005
$N_{\text{H}}^{\text{nucl.}}$	$\alpha_{\text{coro.}}$	0.786	0.004
$N_{\text{H}}^{\text{nucl.}}$	$\log \xi_{\text{AD}}$	0.492	0.124
$N_{\text{H}}^{\text{nucl.}}$	β_{AD}	-0.287	0.392
β_{AD}	$\log \xi_{\text{AD}}$	0.412	0.208
$\log \xi_{\text{AD}}$	$\alpha_{\text{coro.}}$	0.398	0.226
β_{AD}	$\alpha_{\text{coro.}}$	-0.325	0.330

[♣] energy flux 2–10 keV calculated with spectrum by CFLUX in XSPEC

4 DISCUSSION AND CONCLUSIONS

In this paper, all the good quality X-ray archival data of NGC 5506 are analyzed simultaneously to obtain the unprecedented combination of high signal-to-noise ratio and broadband energy coverage for the precise measurement of the black hole spin. There have been several spin measurements for the SMBHs of AGNs through characterizing the relativistic reflection spectra in X-ray (Walton et al. 2013; Tan et al. 2012; Lohfink et al. 2012; Zoghbi et al. 2010). For NGC 5506, the SMBH spin had not been measured. In a previous study on NGC 5506 (Guainazzi et al. 2010b), the data quality (on a smaller data set than discussed in this paper) did not allow to constrain the spin: varying the black hole spin from Schwarzschild to maximally rotating yields a variation of the χ^2 lower than 0.5. In this paper, we constrain the black hole spin to $a = 0.97 \pm_{0.010}^{0.0082}$ at 90% confidence level for one interesting parameter. There have been several measurements where uncertainties in the spin parameter were estimated by 1-D confidence contours, reporting uncertainty ranges of 90% confidence between 0.01 and 1 (e.g. Reynolds (2014)); in this paper, the uncertainty range is 0.018. In Fig. 7, the SMBH mass-spin distribution of NGC 5506 with that of other AGNs collected in Reynolds (2014) are compared. There is a trend, whereby smaller black hole masses correspond to higher black hole

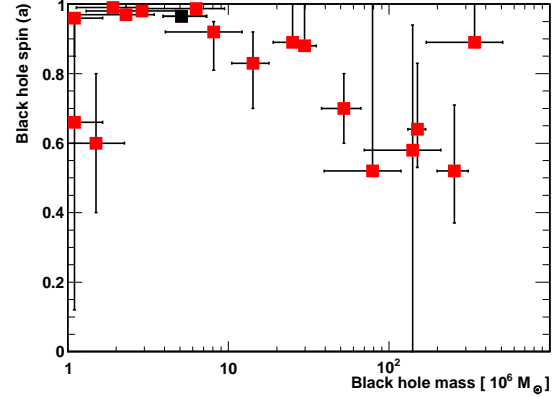


Figure 7. Black hole mass/spin measurements of NGC 5506 (in black; Nikolajuk et al. (2009)/this paper) and other AGNs (in red; data collected in Reynolds (2014)).

Table 8. Constant-function fitting to epoch-dependent parameters.

parameter	$\chi^2 n.d.f.$	p-value
$N_{\text{H}}^{\text{nucl.}}$	(2.46 × 10 ³)/11	0.00
β_{AD}	(8.15 × 10 ¹)/11	2.59 × 10 ⁻¹³
$\alpha_{\text{coro.}}$	(4.93 × 10 ¹)/11	3.62 × 10 ⁻⁷
$\log \xi_{\text{AD}}$	(2.61 × 10 ³)/11	0.00

number of entries: 11 (epochs)

number of parameter: 1 (constant-function)

See description for each parameter in Subsect. 3.2.

spin. While the statistics is still small, NGC5506 agrees with this trend.

In our model, five parameters are epoch-dependent: $N_{\text{H}}^{\text{nucl.}}$, β_{AD} , $\log \xi_{\text{AD}}$, $\alpha_{\text{coro.}}$, and $N_0^{\text{RELX.}}$. They are all variable over time scales probed by our data (see Tab. 6).

In the correlation study (see Tab. 7), there are three correlations significant at a level better than 2%. The $N_{\text{H}}^{\text{nucl.}}$ versus $\alpha_{\text{coro.}}$ is an intrinsic degeneracy between these parameters in the fit. The flux versus index of the radial emissivity profile, and flux versus ionization parameter anti-correlations may suggest that something in the accretion flow changes with flux. A working hypothesis is that what changes is the location of the innermost stable orbit due to over-ionisation of the innermost regions of the disk. At higher fluxes, a wider area of the innermost disk is fully ionized and does not contribute to the reflection. If this happens, the relative weight of disk regions increases that correspond a lower index of the radial emissivity profile and to a lower ionization level (i.e., ionization parameter). Hence it came the idea of changing slightly the baseline model, assuming a constant index of the radial emissivity profile (3), and allowing the radius of the innermost stable orbit (r_{in}) to vary at different epochs (*modified model* hereafter). If this working hypothesis is correct, we should see a positive correlation between flux and r_{in} , and this is indeed what the modified model shows. See Fig. 8. The resulted r_{in} has a Spearman’s correlation coefficient 0.754 with energy flux (a confidence level of 99%). While formally there is a statistical linear correlation between energy flux and $\log r_{\text{in}}$, at high flux levels ($> 9 \times 10^{11}$ cgs) two out of five data points are consistent to those measured at low flux levels. More than a linear correlation, there seems to be a special “high flux state” ($r_{\text{in}} > 10 r_{\text{g}}$) where the properties of the accretion flow differ from

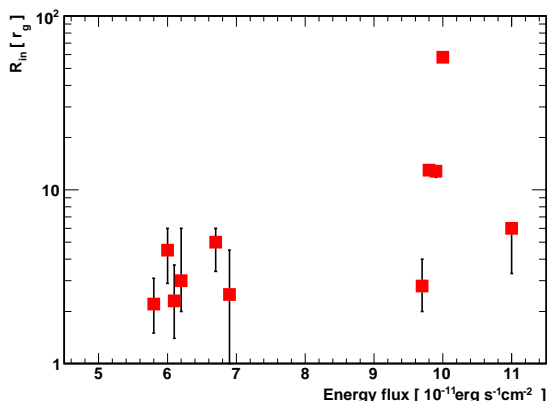


Figure 8. Correlation between energy flux and r_{in} in the *modified model* (see the description in Sect. 4).

any other flux state. These three data points with $r_{\text{in}} > 10r_{\text{g}}$ correspond to epochs 7, 8, and 9 when *Suzaku* observed NGC 5506.

In this modified model, our spectral modeling is inconsistent: the measurement of the black hole spin assumes that the disk reflection is produced down to the ISCO at all epochs. Therefore, we checked its impact on the determination of the spin: $a = 0.93 \pm_{0.016}^{0.0063}$ (in the modified model) at 90% confidence level for one interesting parameter, which is slightly lower than $a = 0.97 \pm_{0.010}^{0.0082}$ in the baseline model. We can see that the statistical accuracy in the measurement of the black hole spin achieved by our study is already excellent, but the *total* uncertainty is larger as reflected in modified model. This uncertainty (i.e., our degree of ignorance of the black hole spin in NGC 5506) is dominated by our ignorance in the physics of the underlying accretion flow, which we have only superficially touched through the modified model. Therefore, the main limitation to relativistic spectroscopy in this moment is due to the uncertainties in the physics, not to the signal-to-noise of the data.

The best-fit nuclear column density varies between 2.8 and $3.4 \times 10^{22} \text{ cm}^{-2}$, i.e. always in the Compton-thin regime. The obscuring matter covering the nucleus, however, has an averaged integrated column density about two orders of magnitude larger. Given the moderate inclination of the system, this suggests that we are looking at the system through a thin atmosphere grazing the surface of the torus.

Our best-fit inclination angles of AD or torus for NLSy1 NGC 5506 are $40^\circ < \theta < 50^\circ$. However, Decarli et al. (2008) assumed low inclination angles ($\lesssim 15^\circ$) and flat geometries of broad-line regions to explain the smaller FWHMs of broad lines in NLSy1. This assumption is different from our fit results. In this case, the ‘narrow’ broad emission lines of NGC 5506 can only be attributed to its smaller SMBH mass, which agrees with the study of Nikolajuk et al. (2009) supporting smaller M_{BH} of NGC 5506.

ACKNOWLEDGMENTS

This work was supported by the NSFC (Grant No. U1531117 and 11305038), Fudan University (Grant No. IDH1512060), and the Thousand Young Talents Program. S.S. also acknowledges support from the AHEAD program for his visit to INAF-Bologna in June 2016. C.B. also acknowledges support from the Alexander von Humboldt Foundation. In this work, the authors used the data

supplied by NASA’s High Energy Astrophysics Science Archive Research Center in the US. The authors also used the data products from the *XMM-Newton*, *Suzaku*, *NuSTAR*, and *Chandra*, funded by the ESA, JAXA, NASA.

REFERENCES

- Arnaud K. A., 1996, in Jacoby G. H., Barnes J., eds, *Astronomical Society of the Pacific Conference Series Vol. 101, Astronomical Data Analysis Software and Systems V*. p. 17
- Ballantyne D. R., Vaughan S., Fabian A. C., 2003, *MNRAS*, **342**, 239
- Bambi C., 2015, preprint, ([arXiv:1509.03884](https://arxiv.org/abs/1509.03884))
- Bardeen J. M., Press W. H., Teukolsky S. A., 1972, *ApJ*, **178**, 347
- Barr P., White N. E., Page C. G., 1985, *MNRAS*, **216**, 65P
- Bianchi S., Balestra I., Matt G., Guainazzi M., Perola G. C., 2003, *A&A*, **402**, 141
- Bianchi S., Miniutti G., Fabian A. C., Iwasawa K., 2005, *MNRAS*, **360**, 380
- Bond I., Matsuoka M., Yamauchi M., 1993, *The Astrophysical Journal*, **405**, 179
- Brenneman L. W., Reynolds C. S., 2006, *ApJ*, **652**, 1028
- Cash W., 1979, *ApJ*, **228**, 939
- Dauser T., García J., Parker M. L., Fabian A. C., Wilms J., 2014, *MNRAS*, **444**, L100
- Dauser T., García J., Walton D. J., Eikmann W., Kallman T., McClintock J., Wilms J., 2016, *A&A*, **590**, A76
- Decarli R., Dotti M., Fontana M., Haardt F., 2008, *MNRAS*, **386**, L15
- Di Matteo T., 1998, *MNRAS*, **299**, L15
- Fabian A. C., Rees M. J., Stella L., White N. E., 1989, *MNRAS*, **238**, 729
- Fabian A. C., et al., 2009, *Nature*, **459**, 540
- Gabriel C., et al., 2004, in Ochenbein F., Allen M. G., Egret D., eds, *Astronomical Society of the Pacific Conference Series Vol. 314, Astronomical Data Analysis Software and Systems (ADASS) XIII*. p. 759
- Galeev A. A., Rosner R., Vaiana G. S., 1979, *ApJ*, **229**, 318
- García J., et al., 2014, *ApJ*, **782**, 76
- George I. M., Fabian A. C., 1991, *MNRAS*, **249**, 352
- González Delgado R. M., Heckman T., Leitherer C., 2001, *ApJ*, **546**, 845
- Grandi P., Tagliaferri G., Giommi P., Barr P., Palumbo G. G. C., 1992, *ApJS*, **82**, 93
- Guainazzi M., Bianchi S., 2007, *MNRAS*, **374**, 1290
- Guainazzi M., Risaliti G., Nucita A., Wang J., Bianchi S., Soria R., Zezas A., 2009, *A&A*, **505**, 589
- Guainazzi M., Bianchi S., Matt G., Dadina M., Kaastra J., Malzac J., Risaliti G., 2010a, *MNRAS*, **406**, 2013
- Guainazzi M., Bianchi S., Matt G., Dadina M., Kaastra J., Malzac J., Risaliti G., 2010b, *Monthly Notices of the Royal Astronomical Society*, **406**, 2013
- Haardt F., Maraschi L., 1991, *ApJ*, **380**, L51
- Haardt F., Maraschi L., Ghisellini G., 1994, *ApJ*, **432**, L95
- Huenemoerder D. P., et al., 2011, *AJ*, **141**, 129
- Jiang J., Bambi C., Steiner J. F., 2015, *ApJ*, **811**, 130
- Kaastra J. S., Bleeker J. A. M., 2016, *A&A*, **587**, A151
- Kallman T., Bautista M., 2001, *ApJS*, **133**, 221
- King A., 2005, *ApJ*, **635**, L121
- Kinkhabwala A., et al., 2002, *ApJ*, **575**, 732
- Komossa S., Xu D., 2007, *ApJ*, **667**, L33
- Laor A., 1991, *ApJ*, **376**, 90
- Lohfink A. M., Reynolds C. S., Miller J. M., Brenneman L. W., Mushotzky R. F., Nowak M. A., Fabian A. C., 2012, *ApJ*, **758**, 67
- Madsen K. K., et al., 2015, *ApJS*, **220**, 8
- Marinucci A., Bianchi S., Nicastro F., Matt G., Goulding A. D., 2012, *ApJ*, **748**, 130
- Matt G., et al., 2015, *MNRAS*, **447**, 3029
- McHardy I. M., Koerding E., Knigge C., Uttley P., Fender R. P., 2006, *Nature*, **444**, 730
- Merloni A., Fabian A. C., 2001, *MNRAS*, **328**, 958
- Miller J. M., 2007, *ARA&A*, **45**, 441

- Murphy K. D., Yaqoob T., 2009, *MNRAS*, **397**, 1549
- Nagar N. M., Oliva E., Marconi A., Maiolino R., 2002, *A&A*, **391**, L21
- Nandra K., Pounds K. A., 1994, *MNRAS*, **268**, 405
- Nandra K., Pounds K. A., Stewart G. C., Fabian A. C., Rees M. J., 1989, *MNRAS*, **236**, 39P
- Nandra K., O'Neill P. M., George I. M., Reeves J. N., 2007, *MNRAS*, **382**, 194
- Nardini E., Fabian A. C., Walton D. J., 2012, *MNRAS*, **423**, 3299
- Netzer H., 2013, *The Physics and Evolution of Active Galactic Nuclei*
- Nikołajuk M., Czerny B., Gurynowicz P., 2009, *MNRAS*, **394**, 2141
- Parker M. L., et al., 2014, *MNRAS*, **443**, 1723
- Pounds K. A., Page K. L., 2005, *MNRAS*, **360**, 1123
- Pounds K. A., Nandra K., Stewart G. C., George I. M., Fabian A. C., 1990, *Nature*, **344**, 132
- Reynolds C. S., 2014, *Space Sci. Rev.*, **183**, 277
- Reynolds C. S., Fabian A. C., 2008, *ApJ*, **675**, 1048
- Reynolds C. S., Nowak M. A., 2003, *Phys. Rep.*, **377**, 389
- Risaliti G., et al., 2013, *Nature*, **494**, 449
- Sako M., Kahn S. M., Paerels F., Liedahl D. A., 2000, *ApJ*, **543**, L115
- Sambruna R. M., Netzer H., Kaspi S., Brandt W. N., Chartas G., Garmire G. P., Nousek J. A., Weaver K. A., 2001, *ApJ*, **546**, L13
- Schurch N. J., Warwick R. S., Griffiths R. E., Kahn S. M., 2004, *MNRAS*, **350**, 1
- Smith R. K., Brickhouse N. S., Liedahl D. A., Raymond J. C., 2001, *ApJ*, **556**, L91
- Storchi-Bergmann T., Fernandes R. C., Schmitt H. R., 1998, *ApJ*, **501**, 94
- Strüder L., et al., 2001, *A&A*, **365**, L18
- Tan Y., Wang J. X., Shu X. W., Zhou Y., 2012, *ApJ*, **747**, L11
- Turner M. J. L., et al., 2001, *A&A*, **365**, L27
- Uttley P., 2007, in Ho L. C., Wang J.-W., eds, *Astronomical Society of the Pacific Conference Series Vol. 373, The Central Engine of Active Galactic Nuclei*. p. 149
- Viegas-Aldrovandi S. M., Contini M., 1989, *ApJ*, **339**, 689
- Walton D. J., Reis R. C., Cackett E. M., Fabian A. C., Miller J. M., 2012, *MNRAS*, **422**, 2510
- Walton D. J., Nardini E., Fabian A. C., Gallo L. C., Reis R. C., 2013, *MNRAS*, **428**, 2901
- Wang T., Mihara T., Otani C., Matsuoka M., Awaki H., 1999, *ApJ*, **515**, 567
- Young A. J., Wilson A. S., Shopbell P. L., 2001, *ApJ*, **556**, 6
- Zoghbi A., Fabian A. C., Uttley P., Miniutti G., Gallo L. C., Reynolds C. S., Miller J. M., Ponti G., 2010, *MNRAS*, **401**, 2419
- Zoghbi A., Reynolds C., Cackett E. M., Miniutti G., Kara E., Fabian A. C., 2013, *ApJ*, **767**, 121